Widely tunable mid-infrared generation via frequency conversion in semiconductor waveguides

Dylan F. Logan,[1] M. Giguere,[2] A. Villeneuve,[2] and Amr S. Helmy[1,*]

[1]*Department of Electrical and Computer Engineering, University of Toronto, 10 King's College Road, Toronto, Ontario M5S 3G4, Canada*

[2]*Genia Photonics Inc., 500 Cartier Blvd. West, Laval, Quebec H7V 5B7, Canada*

**Corresponding author: a.helmty@utoronto.ca*

Received July 24, 2013; revised September 22, 2013; accepted September 28, 2013;
posted October 11, 2013 (Doc. ID 194465); published October 31, 2013

Phase matching in a multilayer AlGaAs waveguide is used to generate mid-IR (7.5–8.5 μm) light through difference frequency generation (DFG) between a 1550 nm pump and 1950 nm signal. This represents the longest wavelength generated through DFG in a 2D waveguide mode in a semiconductor waveguide. It was produced with an efficiency of 1.2×10^{-4} %/W in a 1 mm long sample. The process is shown to be tunable across >2 μm through appropriate tuning of the input pump and signal wavelengths and/or waveguide geometry, and is therefore a viable platform for monolithic, tunable, mid-IR sources. © 2013 Optical Society of America

OCIS codes: (190.4975) Parametric processes; (230.4320) Nonlinear optical devices; (130.7405) Wavelength conversion devices.

http://dx.doi.org/10.1364/OL.38.004457

Generation of mid-infrared and far-infrared (IR) radiation using second-order optical nonlinearities is attractive as it enables simultaneous access of several spectral regions for sensing applications. Such multispectral window coverage is unavailable using conventional lasers, as multiple sources need to be used. This is of particular interest to applications requiring analysis of multiple gases, which demands a wide spectral tuning range that encompasses the signature absorption lines of several gas molecules.

To date, inventions that use second-order nonlinearities are not amenable to monolithic integration with active and passive photonic components. Most popular nonlinear crystals, including lithium niobate ($LiNbO_3$), potassium titanate phosphate (KTP), and barium borate (BBO), do not lend themselves to the monolithic integration with laser pumps. More importantly, the wavelength coverage of oxide-based crystals is limited to below 4–5 μm [1]. The second atmospheric window (7.6–16 μm) has not yet been addressed using frequency conversion in semiconductor waveguides. It has, however, been successfully exploited using quantum cascade lasers (QCLs), which operate from 3.4 to 24 μm. High-power distributed feedback laser QCLs have limited temperature tuning of ~40 nm, and can achieve extended spectral coverage of 2–3 μm by adopting cavity arrays or an external cavity approach [2].

A promising material for on-chip frequency conversion is GaAs/AlGaAs. It benefits from a large transparency window extending to the infrared. By tuning the Al composition, the wavelength range between 0.9 and 17 μm can be covered. GaAs/AlGaAs also has excellent thermal properties, large optical nonlinearities, large optical damage threshold, and mature fabrication technology [3]. This route has been slow to provide alternative sources of infrared radiation due, in part, to the difficulty in phase matching (PM) second-order nonlinearities in semiconductors [3]. In addition, their efficiency has not kept up with the advances in tunability and the power attainable from QCLs [2]. To date, the longest wavelength generated in a guided mode in this material system is 5.6 μm, in a selectively oxidized GaAs–AlAs waveguide [4]. Tunable emissions from 6.7 to 12.7 μm [5,6] and optical parametric oscillation at 4.5 μm [7] have been demonstrated in nonguided orientation patterned GaAs.

Bragg reflection waveguides (BRWs) are a class of waveguides with leaky, low-loss propagating modes. Because waveguiding takes place through Bragg reflection, the waveguide dispersion of this class of waveguides can be very versatile [8]. PM using BRWs utilizes these dispersion properties to match the propagation contacts of the various interacting waves in a DFG process. Through appropriate waveguide design, it is possible to obtain exact PM without the assistance of a grating to compensate for the momentum mismatch. PM using BRWs has been used to achieve second-harmonic generation with conversion efficiency of over $10,000$ %/W cm^2 using picosecond pulses [9]. Wide band sum-frequency generation [10] and difference frequency generation (DFG) [11] with bandwidths well in excess of 100 nm have been obtained at 1550 nm. In addition to the frequency conversion, BRW diode lasers have also been demonstrated [12]. These developments indicate that this class of waveguides is a candidate for self-pumped DFG devices. In this Letter, we extend the design of the BRW PM approach to generate frequencies in the mid-IR using pulsed (100 ps) pump and signal in the near-IR.

The AlGaAs multilayer waveguide structure was designed to support a Type-II DFG process between a TE-polarized pump mode with wavelength in the region of 1550 nm and a TM-polarized signal mode in the region of 1950 nm, to produce a TE-polarized idler around 7.5 μm wavelength. The multilayer structure was designed to support a BRW mode at 1550 nm to serve as the pump, which was dispersion engineered to satisfy exact modal PM with the fundamental signal and idler modes at the desired wavelengths:

$$\Delta\beta = 2\pi\left(\frac{n_{\text{eff}}^{p}(\lambda_p)}{\lambda_p} - \frac{n_{\text{eff}}^{s}(\lambda_s)}{\lambda_s} - \frac{n_{\text{eff}}^{i}(\lambda_i)}{\lambda_i}\right) = 0, \quad (1)$$

where $\Delta\beta$ is the wavenumber mismatch; n_{eff}^{p}, n_{eff}^{s}, and n_{eff}^{i} are the modal indices of the pump, signal, and idler mode,

respectively; and λ_p, λ_s, and λ_i are their respective wavelengths [13]. The ability to control the waveguide dispersive properties enables wide spectral tuning of the idler.

The epistructure was grown by MOCVD (Metal Organic Chemical Vapor Deposition) and had a thickness of 16.5 μm. Al compositions were limited to 21%–61% to minimize losses associated with free-carrier absorption. A 7.3 μm thick low index (61% Al) clad layer was used to confine the long-wavelength idler mode. The structure consisted of a dual-layer core, a matching layer (ML), and a two-period Bragg Reflector stack. The layer thicknesses were designed to satisfy the PM condition of Eq. (1), and the resulting set of solutions were evaluated to maximize the overlap integral of the modes and the effective nonlinear coefficient of the structure. The details of the BRW design process for PM using the ML can be found in [9]. The design used is illustrated in Fig. 1(a), and the interacting pump, signal, and idler modes are depicted in Fig. 1(b). The spatial overlap between modes is intrinsically limited by the multilobed BRW mode shape and the disparity between interacting wavelengths. Here, the core thicknesses were chosen to extend the peak intensity of the pump and signal modes into the thicker ML layer, to enhance the overlap with the broader idler mode profile. The nonlinear coefficient of the layer with 21% Al composition has a strength of 11 pm/V.

The waveguides were characterized with a Genia MOPA C-band laser as the TE-polarized pump source and a Genia Programmable Laser as the TM-polarized signal source. These laser sources were synchronized with a repetition rate of 15.2 MHz and a 100 ps pulse width. A polarization beam splitter cube was used to mix the pump and signal. A Newport 40× objective lens was used to couple light into the waveguide, and the transmitted light was collected by an Innovation Photonics 0.25NA ZnSe objective lens with 7.5–9.5 μm antireflection coating. The generated idler was focused onto an Infrared Associates Mercury Cadmium Telluride (MCT) photodetector, through two long-wavelength pass filters with 5.5 μm cutoff to reject the pump and signal.

The coupling into the BRW mode is ~4%, owing to the significant modal mismatch. The insertion loss of the pump and signal modes are estimated to be 21.8 and 3.7 dB, respectively.

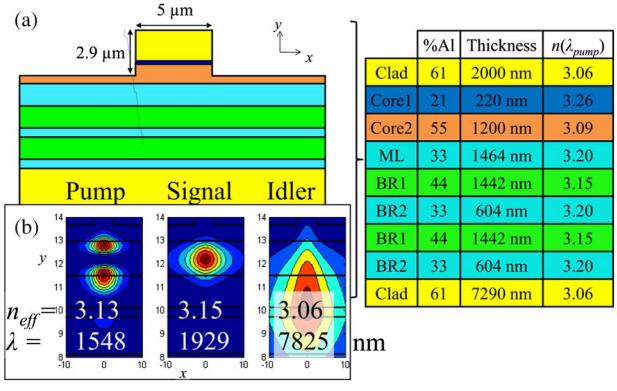

	%Al	Thickness	$n(\lambda_{pump})$
Clad	61	2000 nm	3.06
Core1	21	220 nm	3.26
Core2	55	1200 nm	3.09
ML	33	1464 nm	3.20
BR1	44	1442 nm	3.15
BR2	33	604 nm	3.20
BR1	44	1442 nm	3.15
BR2	33	604 nm	3.20
Clad	61	7290 nm	3.06

Fig. 1. (a) Schematic and description of the waveguide under test and (b) simulated mode field profiles of the three interacting modes.

Figure 2(a) plots the power measured on the MCT detector (P_i) as a function of pump wavelength λ_p at fixed coupled average power of 1.6 mW, while the signal wavelength was fixed at $\lambda_s = 1949.38$ nm at an on-chip average power of 41.3 mW. Two peaks were observed: one at $\lambda_p = 1552.5$ nm (2), and another just outside of the tuning range of the C-band source (1). The pump was fixed at $\lambda_p = 1563.5$ (the upper limit of the C-band tuning range), and λ_s was tuned to investigate peak (1) via a signal tuning curve, shown in Fig. 2(b). The idler power reached a level of $P_i = 55$ nW at a signal wavelength of $\lambda_s = 1925.2$ nm. The pump was then fixed at $\lambda_p = 1552.5$ nm and λ_s was varied to investigate peak (2), yielding a maximum power of $P_i = 12$ nW at $\lambda_s = 1942$ nm.

The linearity of the transmitted power with both injected pump and signal power levels was ensured to confirm that two-photon absorption effects are not taking place. Neglecting the idler collection efficiency, an efficiency of approximately $\eta = 1.2 \times 10^{-4}$ %/W was obtained using the expression $\eta = P_i/(P_p P_s) \times f_{\text{rep}}\tau$, where f_{rep} is the repetition rate (15.2 MHz) and τ is the pulse width (100 ps) of the two lasers. The propagation losses in the modes limit the conversion efficiency, and may be reduced by improving etch sidewall quality and therefore reducing scattering loss. For instance, for a 5 dB/cm loss in each mode, the efficiency is calculated to be 9×10^{-3} %/W, comparable to the values reported for selectively oxidized GaAs–AlAs waveguides [4]. In addition, deeply etched structures may be used to improve the spatial overlap of the three modes through stronger lateral confinement, which is weak as shown in Fig. 1(b). Note also that P_i is the power detected by the MCT detector, so the estimate above doesn't take into account the idler collection efficiency. The pump and signal had Gaussian-shaped spectra, with FWHM of 0.1 nm and 0.7 nm, respectively. As a result, the idler spectral width

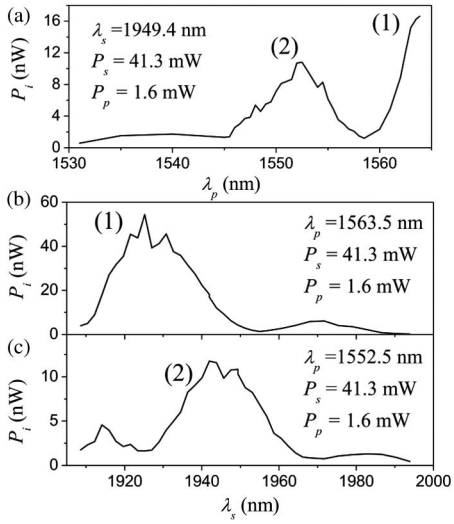

Fig. 2. (a) Pump tuning curve: variation of idler power P_i as input pump wavelength λ_p is varied across its 1531–1563.5 nm tuning range for a constant signal wavelength $\lambda_s = 1949.4$ nm. Signal tuning curves: variation of P_i as input signal wavelength λ_s is varied across its 1908.5–1994 nm tuning range for a constant pump wavelength of (b) $\lambda_p = 1563.5$ nm and (c) $\lambda_p = 1552.5$ nm.

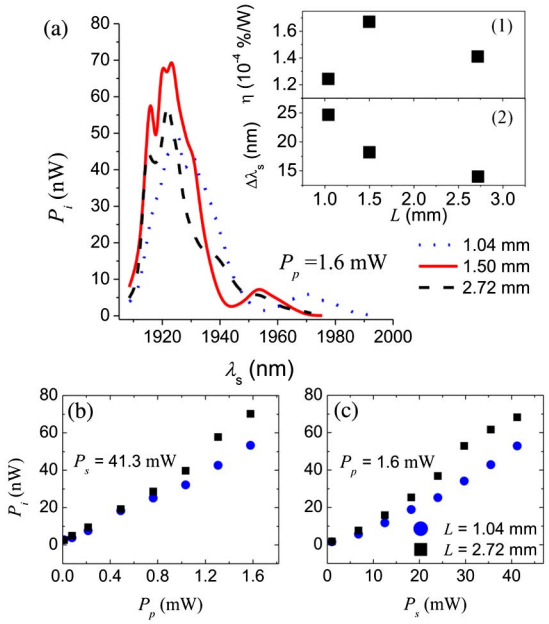

Fig. 3. (a) Signal tuning curve for three waveguide lengths L; Inset 1, estimated efficiency η (%/W) versus L; Inset 2, phase-matched signal bandwidth versus L (b) P_i versus input pump power P_p. (c) P_i versus input signal power P_s.

is estimated to be 2.1 nm, the convolution of the source spectral widths.

This process was undertaken for three sample lengths, and the signal tuning curves of peak (1) are shown in Fig. 3. The inset plots the extracted efficiency η versus length L, and yields values that are equal within uncertainty over this length range, rather than the expected quadratic dependence [10]. For the longer pulse widths used here (100 ps), group velocity mismatch can be ruled out as a limiting factor for the scaling of the efficiency with lengths, as the walk off length of this pulse width is $\sim L = 200$ cm. The PM bandwidth is also provided in an inset plot. Considering the dispersion of the interacting modes, the PM bandwidth for the signal at $L = 1$ mm is calculated to be 17 nm, and is in reasonable agreement with the measured value.

Figures 3(b) and 3(c) plot P_i with only P_s and P_p varied, respectively, while the other is fixed, and exhibit the linear dependence expected for a DFG process. The exception is that, in the longer waveguide, the characteristic in Fig. 3(c) becomes sublinear for signal powers greater than 30 mW, indicating that the process is being limited by the available on-chip pump power in the BRW mode. The measured power is reduced to zero when either the pump or signal is removed, confirming that neither are independently contributing to P_i.

For peaks (1) and (2) in Fig. 2, a series of signal tuning curves were produced for different pump wavelengths in order to generate a set of PM wavelength pairs. The set of points (λ_p, λ_s) for each peak are plotted in Fig. 4 along with the inferred idler wavelength λ_i, and indicate micrometers of tuning range available in mid-IR generation.

The simulated $\Delta\beta$ of the interaction between the three slab modes and three ridge modes is plotted in Fig. 4(b) for a fixed $\lambda_s = 1950$ nm. The ridge modes are PM for $\lambda_p = 1556$ nm, while the slab modes are PM for $\lambda_p = 1543$ nm. The PM curves of these simulations are

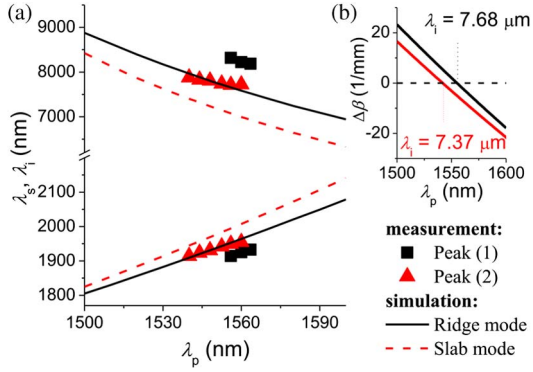

Fig. 4. (a) Phase-matched curve simulated for interaction between ridge modes and slab modes of the waveguide (lines) and measured points for peak (1) and (2); (b) simulated phase-matched solution $\Delta\beta = 0$ [see Eq. (1)] for $\lambda_s = 1950$ nm for both ridge and slab modes, denoting generated wavelengths λ_i.

plotted as black and red lines in Fig. 4(a). This shift in PM wavelength between ridge and slab mode simulations is similar to that observed between peak (1) and (2) in measurement, and we therefore believe that the slab mode interaction is responsible for the weaker peak (2). There are no higher-order modes supported by the structure that could interact to provide the second set of peaks. The measured PM points are shifted significantly from the simulated curves. This is likely caused by the 3% uncertainty in Al fraction in the wafer growth as well as deficiencies in the refractive index models at mid-IR wavelengths.

From the ridge modes alone, the idler can be tuned from 6.9 to 8.9 μm by tuning λ_p from 1500 to 1600 nm and λ_s from 1800 to 2100 nm. Therefore, this single substrate can be deployed to generate a broad range of mid-IR frequencies. The additional parameter in dispersion engineering is the waveguide geometry. The signal tuning curve for a sample with an etch depth (d) of 2.5 μm is plotted in Fig. 5(a), along with the curve for $d = 2.9$ μm of Fig. 2, for fixed pump and signal average in-coupled powers of 14.3 and 1.6 mW, respectively. The dispersion controls the PM signal wavelength λ_s predicted by Eq. (1).

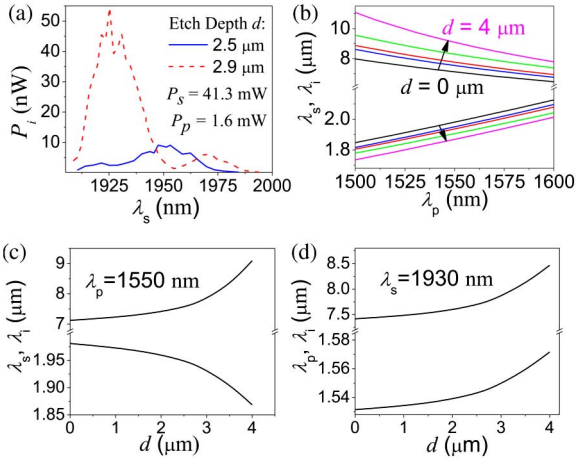

Fig. 5. (a) Signal power tuning curve of two waveguide geometries; (b) simulated phase-matched curves for varied etch depth d; (c) simulated phase-matched curve for fixed pump and varied signal wavelength and etch depth; (d) simulated phase-matched curve for fixed signal and varied pump wavelength and d.

The simulated tuning of the structure as etch depth d is varied is shown in Fig. 5(b), illustrating this added route for tunability.

The full potential of this technique is illustrated in Figs. 5(c) and 5(d), where large tuning range is provided with variation of one input wavelength only. In Fig. 5(c), λ_p is fixed while etch depth d and λ_s are varied to produce an idler tuning range of >2 μm. In Fig. 5(d), λ_s is instead fixed and λ_p is varied along with d, demonstrating that a fixed signal wavelength and a pump wavelength tunable across the C-band can produce >2 μm of idler tuning on this substrate. This is competitive with the tunability provided by external cavity QCLs [2].

In summary, we have demonstrated a platform for the generation of a widely tunable mid-IR radiation using a single multilayer waveguide using DFG. The structure represents, to our knowledge, the longest wavelength generated in a semiconductor waveguide using DFG. Tuning ranges of >2 μm were shown to be feasible with room for extending this range. This forms a platform for self-pumped, widely tunable mid-IR generation, amenable to integration with other waveguide components.

References

1. V. Petrov, Opt. Mater. **34**, 536 (2012).
2. Y. Yao, A. J. Hoffman, and C. F. Gmachl, Nat. Photonics **6**, 432 (2012).
3. A. S. Helmy, P. Abolghasem, J. S. Aitchison, B. J. Bijlani, J. Han, B. M. Holmes, D. C. Hutchings, U. Younis, and S. J. Wagner, Laser Photon. Rev. **5**, 272 (2011).
4. P. Bravetti, A. Fiore, V. Berger, E. Rosencher, and J. Nagle, Opt. Lett. **23**, 331 (1998).
5. K. L. Vodopyanov, O. Levi, P. S. Kuo, T. J. Pinguet, J. S. Harris, M. M. Fejer, B. Gerard, L. Becouarn, and E. Lallier, Opt. Lett. **29**, 1912 (2004).
6. C. R. Phillips, J. Jiang, C. Mohr, A. C. Lin, C. Langrock, M. Snure, D. Bliss, M. Zhu, I. Hartl, J. S. Harris, M. E. Fermann, and M. M. Fejer, Opt. Lett. **37**, 2928 (2012).
7. M. B. Oron, P. Blau, S. Pearl, and M. Katz, Proc. SPIE **8240**, 82400C-1 (2012).
8. A. Y. Cho, A. Yariv, and P. Yeh, Appl. Phys. Lett. **30**, 471 (1977).
9. P. Abolghasem, J. Han, B. Bijlai, A. Arjmand, and A. S. Helmy, IEEE Photon. Technol. Lett. **21**, 1462 (2009).
10. J. Han, P. Abolghasem, B. Bijlani, and A. S. Helmy, Opt. Lett. **34**, 3656 (2009).
11. J. Han, P. Abolghasem, D. P. Kang, B. J. Bijlani, and A. S. Helmy, Opt. Lett. **35**, 2334 (2010).
12. B. Bijlani and A. S. Helmy, Opt. Lett. **34**, 3734 (2009).
13. T. Suhara and M. Fujimura, *Waveguide Nonlinear-Optic Devices* (Springer, 2003).